The climatology of carbon monoxide and water vapor on Mars as observed by CRISM and modeled by the GEM-Mars general circulation model

Michael D. Smith [a,*], Frank Daerden [b], Lori Neary [b], Alain Khayat [c,a]

[a] *NASA Goddard Space Flight Center, Greenbelt, MD 20771, United States*
[b] *Royal Belgian Institute for Space Aeronomy, Brussels, Belgium*
[c] *University of Maryland, College Park, MD 20742, United States*

ABSTRACT

Radiative transfer modeling of near-infrared spectra taken by the Compact Reconnaissance Imaging Spectrometer for Mars (CRISM) instrument onboard Mars Reconnaissance Orbiter (MRO) enables the column-integrated abundance of carbon monoxide (CO) and water vapor (H_2O) to be retrieved. These results provide a detailed global description of the seasonal and spatial distribution of CO in the Mars atmosphere and new information about the interannual variability of H_2O. The CRISM retrievals show the seasonally and globally averaged carbon monoxide mixing ratio to be near 800 ppm, but with strong seasonal variations, especially at high latitudes. At low latitudes, the carbon monoxide mixing ratio varies in response to the mean seasonal cycle of surface pressure and shows little variation with topography. At high latitudes, carbon monoxide is depleted in the summer hemisphere by a factor of two or more, while in the winter hemisphere there is relatively higher mixing ratio in regions with low-lying topography. Water vapor shows only modest interannual variations, with the largest observed difference being unusually dry conditions in the wake of the Mars Year 28 global dust storm. Modeling results from the GEM-Mars general circulation model generally reproduce the observed seasonal and spatial trends and provide insight into the underlying physical processes.

Published by Elsevier Inc.

1. Introduction

Water vapor has long been recognized as a key constituent for understanding a wide range of physical processes in the Mars atmosphere, and there is now a long history of spacecraft observations of water vapor at Mars. Retrievals of water vapor column using data from the Viking Orbiters (Jakosky and Farmer, 1982), Mars Global Surveyor (Smith, 2002, 2004), Mars Express (e.g., Melchiorri et al., 2007; Fouchet et al., 2007; Tschimmel et al., 2008; Maltagliati et al., 2008, 2011; Fedorova et al., 2006; Trokhimovskiy et al., 2015), and Mars Reconnaissance Orbiter (Smith et al., 2009) have provided a baseline of observations that characterize the major seasonal and spatial variations. These observations have shown some variations between different Mars Years, but continued observations by current and future spacecraft (including those presented here) are helpful to better characterize interannual variability.

Carbon monoxide plays a major role in the martian photochemical cycle of CO_2, and is a tracer of the middle atmosphere thermal profile and winds. CO is also a non-condensable species for which local and temporal variations are expected over the martian seasons. Therefore, the spatial distribution of CO as a function of season is an important quantity that provides sensitive constraints on models of photochemical and dynamical processes in the Martian atmosphere. Compared with water vapor, there have been relatively few retrievals of CO. Ground-based (e.g., Clancy et al., 1990; Lellouch et al., 1991; Krasnopolsky, 2003,2007) and spacecraft-based (e.g., Encrenaz et al., 2006, Billebaud et al., 2009; Smith et al., 2009) observations have produced limited information about the seasonal and spatial variations, but a detailed climatology has not previously been established.

Near-infrared spectra taken by the Compact Reconnaissance Imaging Spectrometer for Mars (CRISM) (Murchie et al., 2007) on-board the Mars Reconnaissance Orbiter (MRO) spacecraft (Zurek and Smrekar, 2007) contain the clear spectral signatures of water vapor and CO gas and are well-suited for retrievals of the column abundance of those gases. Initial retrievals of water vapor and CO using CRISM observations covering one Martian Year

* Corresponding author.
E-mail address: michael.d.smith@nasa.gov (M.D. Smith).

were reported by Smith et al. (2009). In this paper we update the results shown in Smith et al. (2009) for the abundance of water vapor and CO using an improved retrieval algorithm to provide retrievals from more than 4 Mars Years of additional CRISM observations covering Mars Year (MY) 28, $L_s = 113°$ to MY 33, $L_s = 286°$. We provide a detailed climatology of CO and use the newly extended baseline of water vapor retrievals to examine interannual variations. We compare the results against the output from a Mars general circulation model (GCM) to provide insight into the physical processes that explain the observed seasonal and spatial trends.

In Section 2, we describe the CRISM instrument and the observations used in this study. In Section 3 we provide details about the retrieval algorithm including the assumptions used and the expected uncertainties in the retrieved quantities. The retrieval results are discussed in Section 4, and in Section 5 we compare the retrieved values against the output from the GEM-Mars GCM model. Finally, we summarize our findings in Section 6.

2. Data set

2.1. CRISM instrument

The Compact Reconnaissance Imaging Spectrometer for Mars (CRISM) is a hyperspectral imager with a spectral range of 362–3920 nm and spatial resolution of 15–19 km/pixel (Murchie et al., 2007). The spectral sampling is 6.55 nm and the spectral resolution in the infrared (∼2300 nm) is about 15 nm. Two detector arrays (covering 362–1056 and 1001–3920 nm) with 640 spatial pixels across track and 480 spectral pixels allow hyperspectral images to be built up using a combination of orbital motion and gimbal movement. The primary spectral sampling modes return either 545 channels ("hyperspectral" observations) at the full instrument spectral resolution, or a 72-channel subset ("multispectral" observations) of the channels chosen to define surface and atmospheric features of interest (Pelkey et al., 2007).

2.2. Observations used for this study

For this study we use all nadir-viewing hyperspectral observations taken with emission angle less than 80°. This includes both images targeted at locations of interest to surface science, and the general mapping observations taken in long strips along the orbit track. The combination of these observation types provide enough coverage to enable a good characterization of the seasonal and global-scale trends of water vapor and carbon monoxide abundance, but are not enough to provide useful maps on time scales of days or weeks.

The processing of the CRISM images is the same as described in Smith et al. (2009). For each image we spatially average the central 100 × 100 pixels of the nadir image to form the spectrum we use in the retrieval. This translates to an area about 2 km square on the surface, which is more than sufficient to characterize the seasonal and regional scale spatial trends that we are interested in. The spatial averaging also reduces random noise in the spectra and minimizes the small change in wavelength for a given spectral channel from one end of the image to the other.

At the wavelengths used in this study (1800–2700 nm) there is negligible contribution from thermal radiation, so we rely on reflected solar light for our signal. This means that we cannot view the winter polar regions. We also wish to avoid the complications of radiative transfer near the limb, so we limit our retrieval to observations with a solar incidence angle of 80° or less. We also do not attempt retrieval on any spectrum that shows the spectral signatures of surface ice (Cull et al., 2010).

The CRISM hyperspectral images included in this study cover the time period from Mars Year (MY) 28, $L_s = 113°$ to MY 33,

$L_s = 286°$ (27 September 2006 to 24 December 2016), or more than 5 Mars Years. Fig. 1 shows the coverage given by the more than 38,000 retrievals. The time coverage during the most recent couple of Mars Years has been reduced because the cryo-cooler needed to take the near-infrared images used for the retrievals described here is only operated during one in every four 2-week planning cycles to conserve the unknown but limited lifetime remaining for the cooler mechanism.

3. Retrieval algorithm

For the retrieval of water vapor and carbon monoxide gas abundance, we focus on the portion of the CRISM spectrum between 1800 and 2700 nm. The main spectral signatures caused by water vapor in the CRISM spectra are centered at roughly 1350, 1900, and 2600 nm. The band at 1350 nm is relatively weak, but the bands at 1900 and 2600 nm are both mixed with stronger carbon dioxide bands on their long-wavelength edges. Our experience with the CRISM spectra is that the band at 2600 nm (which is the strongest of the three) provides the most reliable retrieval (Smith et al., 2009). Carbon monoxide has a readily apparent spectral signature centered near 2350 nm. Although this band is weak, it is isolated from other atmospheric spectral signatures and still provides reliable retrievals. Retrieval of carbon dioxide is included in the algorithm to provide a measure of total atmospheric column for the calculation of the volume mixing ratio. As the main constituent of the atmosphere, carbon dioxide has numerous strong spectral signatures throughout the CRISM spectral range including prominent bands centered near wavelengths of 1400, 2000, and 2700 nm. We choose to use the band centered near 2000 nm for our retrieval of carbon dioxide abundance because it provides the best balance between having sufficient strength to provide good signal, while not being so strong that the band is completely saturated.

3.1. Radiative transfer and assumptions

The radiative transfer modeling and algorithm used here for the retrieval of water vapor and carbon monoxide is essentially the same as that described in Smith et al. (2009) with a few improvements. Radiative transfer modeling is used to compute an expected spectrum for a given abundance of water vapor, carbon monoxide, and carbon dioxide, and those gas abundances are varied until the resulting computed spectrum best matches the observed spectrum in a least-squares sense.

We compute synthetic spectra using the correlated-k approximation for gas absorption (Lacis and Oinas, 1991) with line parameters from the HITRAN 2012 spectroscopic database (Rothman et al., 2013). Aerosol scattering and the direct solar beam are treated using the discrete ordinates approach (e.g., Goody and Yung, 1989; Thomas and Stamnes, 1999). The viewing geometry, including the solar incidence angle, emission angle, and distance between Mars and the Sun, is taken from spacecraft records and is assumed to be known. The solar spectrum used is the one adopted by the CRISM team, which is taken from the terrestrial MOD-TRAN atmospheric radiation code (Berk et al., 1998). Atmospheric temperatures (which affect the modeled gas absorption) are taken from TES climatology (Smith, 2004). Surface pressure is computed using the retrieved abundance of carbon dioxide and an assumed CO_2 volume mixing ratio of 0.96 based on measurements by the *Curiosity* rover (Mahaffy et al., 2013). The vertical distribution of carbon monoxide is assumed to be well mixed. Water vapor is assumed to be well mixed up to the water condensation level and then to follow the water saturation curve above that.

Dust and water ice aerosols affect the observed strength of gas absorption features and so aerosols must be included in the
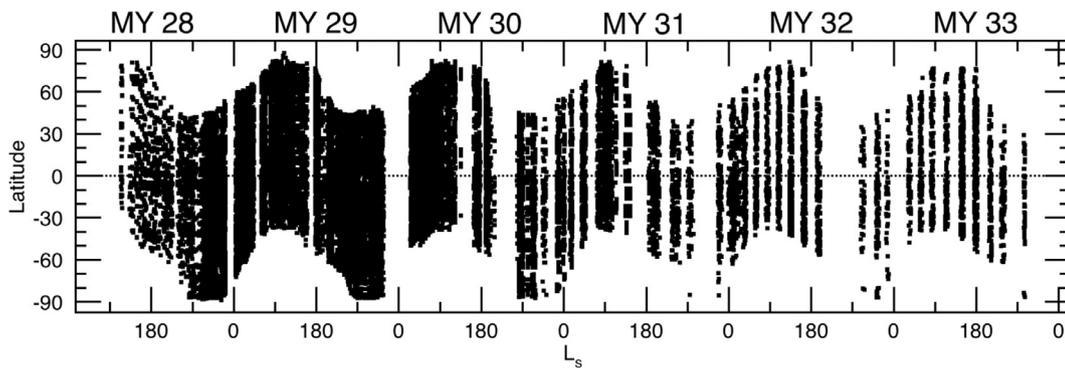
Fig. 1. The seasonal and latitudinal coverage of the CRISM hyperspectral observations used in this study.

model. Aerosol optical depth is estimated for each CRISM observation using retrievals from concurrent observations from Mars Odyssey THEMIS (Smith et al., 2009). Aerosol size (effective radius of 1.5 μm for dust and 2.0 μm for water ice) is taken from modeling of the spectral dependence of dust absorption in TES spectra (Wolff and Clancy, 2003) and from multi-wavelength comparisons of TES, mini-TES, and CRISM spectra (Clancy et al., 2003; Wolff et al., 2006, 2009). Aerosol scattering properties are taken from the detailed modeling of CRISM emission phase function spectra, where the same spot on the surface is observed at a number of different emission angles as the spacecraft flies overhead (Wolff et al., 2009). Dust is assumed to be well mixed with the background gas, while water ice clouds are assumed to be well mixed above the water condensation level with no cloud below.

3.2. Retrieval algorithm process and improvements

As described in Smith et al. (2009), the retrievals for gas abundance are performed sequentially since although CO and H_2O do not affect the CO_2 absorptions, CO_2 does affect the H_2O absorption and H_2O affects the CO absorption. The first step then is to retrieve CO_2 abundance using 12 CRISM spectral channels between 1961 and 2080 nm that describe the characteristic "triplet" structure of the CO_2 absorption feature and surrounding continuum level. This also allows a wavelength calibration to be retrieved. We model the wavelength calibration in a simple way as a single additive offset to the nominal wavelength of all CRISM channels. This offset is generally small (less than 1 nm) and is roughly related to instrument temperatures.

Given the retrieved CO_2 abundance (and thus, surface pressure), we next move to the retrieval of water vapor. Twelve CRISM channels between 2549 and 2635 nm are used in the retrieval. Because the high wavelength edge of the H_2O band is overwhelmed by a very strong CO_2 band centered near 2700 nm, a continuum level on the high wavelength side of the band cannot be established and instead we fit for a slope in the background continuum level. The height of the water condensation depends on the retrieved abundance of H_2O, so the retrieval is iterated until convergence.

Finally, given the retrieved surface pressure and H_2O abundance we now retrieve the CO abundance. Since the CO band is very weak and is also relatively weakly dependent on the on the abundance of CO, it is important to have the best estimates possible for all other quantities first. The high wavelength side of the CO band has a small but still noticeable contribution from water vapor absorption, which is taken into account using the previously retrieved H_2O abundance. A total of 17 CRISM channels between 2285 and 2457 nm are used in the retrieval.

Fig. 2 shows the result of the retrieval for the CRISM observation HRL0000515F (MY 28, $L_s = 211°$; 9°S latitude, 293°W longitude). The retrieved values are a surface pressure of 7.3 mbar,
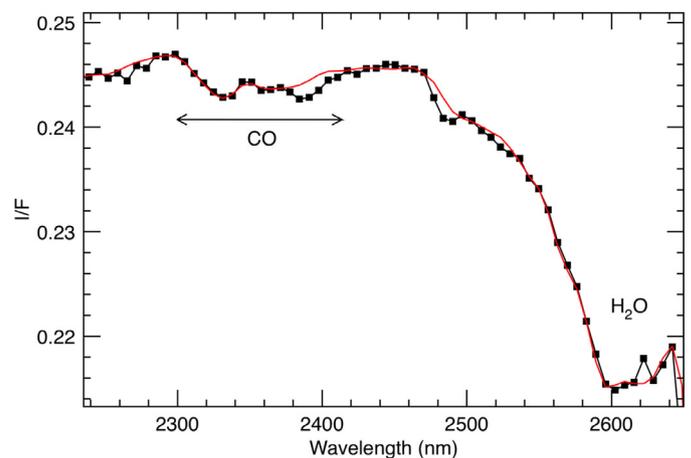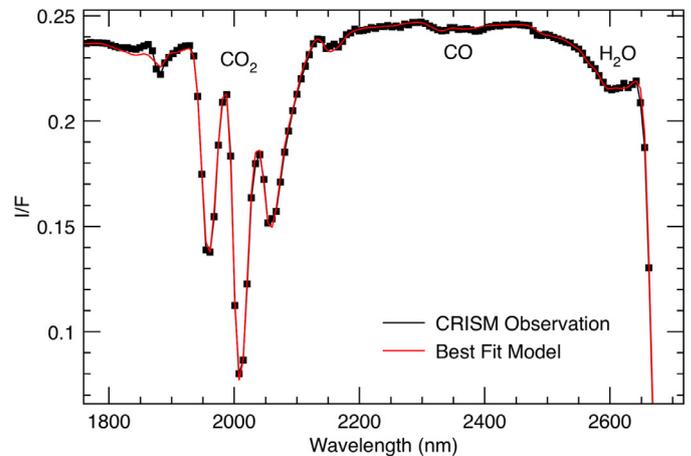
Fig. 2. A portion of a typical CRISM spectrum (HRL0000515F; $L_s = 211°$, 9°S, 193°W) used in the retrieval. Spectral features caused by CO_2, CO, and H_2O are labeled. The best fit computed spectrum (red) is compared against the CRISM observation (black). The retrieved values are a surface pressure of 7.3 mbar, 15 precipitable microns (pr-μm) water vapor, and 880 ppm carbon monoxide. (For interpretation of the references to color in this figure legend, the reader is referred to the web version of this article.)

15 precipitable microns (pr-μm) water vapor, and 880 ppm carbon monoxide. The quality of this fit is very good. We reject any retrieval with parameters outside reasonable bounds (e.g., surface pressure greater than 15 mbar), or whose fit is poor as determined by the RMS difference between observed and best fit computed radiance. A poor fit is defined as the 5% of retrievals having the highest RMS radiance differences.

The improvements to the retrieval algorithm used by Smith et al. (2009) are in the choice of the specific CRISM spectral channels used in the retrievals for CO and H$_2$O. In each case, after careful study of the residuals for many thousands of retrievals some of the spectral channels used were changed to better describe the spectral shapes being fit. For CO, the channels between 2340 and 2405 nm were removed from the retrieval because those channels very often did not fit as well as neighboring channels (see mismatch in bottom panel of Fig. 2, for example). The net result of these improvements was a small improvement in retrieval uncertainties and a reduction in the number of outliers and the spatial variations observed in CO mixing ratio.

3.3. Uncertainties

The uncertainties in retrieved results for this retrieval algorithm were described in some detail by Smith et al. (2009), and are summarized again here. The dominant source of uncertainty in the retrieval is related to the systematic errors in the assumptions and approximations used in the retrieval process. These uncertainties are most easily estimated through numerical experiments. For each source of uncertainty, the retrieval can be run under a range of different assumptions or approximations to evaluate the resulting change to the retrieved gas abundances.

One assumption is the use of aerosol optical depths retrieved from concurrent THEMIS observations instead of from the CRISM observations themselves. Numerical experiments show that doubling the typical aerosol optical depth found outside of major dust storms leads to changes in the retrieved gas abundances of 1% for H$_2$O and 3% for CO. As long as the THEMIS observations are able to give generally accurate aerosol optical depth and to determine when and where large dust storms occur, the uncertainty from this source will be small. During a major dust storm the optical depth of dust can become large enough to screen the lower atmosphere and the entire column is not sampled by the CRISM observations. To prevent this, we exclude any observation taken when the dust optical depth at CRISM wavelengths is greater than unity. A related assumption is our use of a well-mixed vertical profile for dust. Numerical experiments show that taking different vertical distributions for the dust causes changes in retrieved quantities no larger than those quoted above.

Another assumption is our use of TES climatology for atmospheric temperatures, which affect the spectroscopic properties of the gases, including line strengths and widths. We expect the atmospheric temperatures obtained from TES climatology to be within 10 K of the true value for almost all cases (Smith, 2004). An offset in the temperature profile by 10 K over the entire atmosphere leads to a change in the retrieved abundances of 15% for H$_2$O and 9% for CO. Because of the dependence of gas spectroscopic properties on atmospheric temperature and pressure, there is also some sensitivity to the vertical distribution of water vapor. Numerical experiments show that changes to our assumed water vapor vertical profile can result in a difference in the retrieved water vapor of up to 10% in extreme cases.

Another assumption is the value used in the retrieval for the CO$_2$ broadening of H$_2$O and CO lines. The broadening coefficients given in the HITRAN database are for terrestrial conditions (i.e., broadened by a nitrogen/oxygen mixture). For simplicity, we use a constant multiplicative factor of 1.5 for water vapor and 1.25 for CO to approximate CO$_2$ broadening. These values compare well with the CO$_2$ broadening coefficients obtained from lab work and theoretical calculations (e.g., Varanasi, 1975; Gamache et al., 1995; Sung and Varanasi, 2005; Brown et al., 2007). We expect the uncertainty associated with this assumption to be small compared to others described here, and in any case would give a nearly
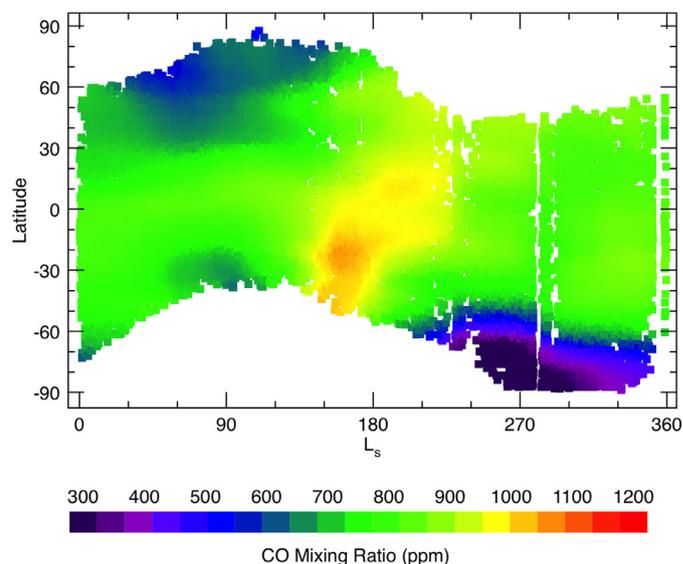
Fig. 3. The seasonal and latitudinal variation of CO mixing ratio as retrieved from CRISM spectra. Smoothing with window size 30° in L$_s$ and 10° in latitude has been applied to the retrievals to better show the trends.

constant overall shift to retrieved values leaving seasonal and spatial patterns unaffected.

Uncertainty related to our approximation of the continuum level is more difficult to test experimentally. However, after having tried numerous different formulations, we believe that the choice of CRISM channels used in the model is a significant but not dominant source of uncertainty, and is more important for weaker spectral signatures. We estimate the uncertainties as 10% for H$_2$O and 20% for CO.

Model-related assumptions, such as the number of vertical layers used in the radiative transfer model, the number of streams used in the discrete ordinates, and the number of terms in the Legendre polynomial expansion of the scattering phase function all lead to small uncertainties compared with other sources. Numerical experiments doubling the number of levels or streams give differences in retrieved results of less than 2%.

Considering all of the above sources of uncertainty, we estimate that the total uncertainty in gas abundance for a single retrieval as 20% for water vapor and 40% for carbon monoxide. Spatial and temporal averaging can reduce these uncertainties somewhat, but some portion of the uncertainty is systematic and does not necessarily average out.

4. Retrieval results

We present here the results of the retrieval of carbon monoxide volume mixing ratio and water vapor column abundance using all nadir-viewing CRISM hyperspectral observations, which span more than 5 Mars Years. Observations with a solar incidence angle greater than 80°, those showing the spectral signature of surface ice, and those with the highest RMS residuals between best fit and computed radiance have been excluded.

4.1. Climatology of retrieved carbon monoxide

Fig. 3 shows the retrieved column volume mixing ratio of carbon monoxide as a function of seasonal date (L$_s$) and latitude averaged for all Mars Years observed. As previously discussed, the uncertainty on individual retrievals of CO mixing ratio is relatively large (40%) because of the weakness of the CO absorption and the relative insensitivity of the observed band depth to CO abundance. Therefore, the CO mixing ratio shown in Fig. 3 has been smoothed

to highlight the climatological trends, which do show clear and repeatable trends as a function of L_s and latitude. The CO mixing ratios presented here are somewhat higher overall than those given by the earlier version of our retrieval (Smith et al., 2009) by about 10–20% on average. Retrievals taken during large dust storms when the dust optical depth at 2300 nm is greater than unity have been excluded from this average because of the increased difficulty in performing a reliable retrieval for gas abundance under conditions of high dust loading.

The summertime polar regions in both hemispheres show significant depletion of CO mixing ratio. The southern hemisphere shows the larger summertime depletion with the retrieved CO mixing ratio falling to nearly 200 ppm poleward of 70°S latitude near the summer solstice ($L_s = 270°$). At a given latitude, it appears that the minimum CO mixing ratio is reached just before solstice and that the recovery in mixing ratio takes an extended period of time. In the northern hemisphere the summertime depletion is less pronounced, but still significant with a minimum retrieved value near 500 ppm somewhat before the summer solstice ($L_s = 90°$). Recovery of CO mixing ratios in the north appears to occur somewhat more quickly than at southern polar latitudes. Because CRISM relies on reflected sunlight to observe spectral features, retrieved CO mixing ratio is not available at polar latitudes during local winter when the Sun is below the horizon. Models show a corresponding enhancement in CO mixing ratio near the winter pole (Section 5.6; Forget et al., 2008), but this is not directly confirmed by the CRISM retrievals.

During the seasons when retrievals exist, carbon monoxide mixing ratio shows a strong latitudinal gradient in the southern hemisphere peaking at about 60°S. Indeed, there is essentially no signature of the summer depletion and winter enhancement pattern observed in the retrievals equatorward of about 50°S latitude. On the other hand, the signature of the summertime depletion in the northern hemisphere extends somewhat further equatorward, as far as about 30°–40°N latitude.

At low latitudes CO mixing ratio varies between an annual minimum of about 725–825 ppm at $L_s = 0°$ to about 1000 ppm in the season around $L_s = 180°$. As shown in Fig. 4, both the annual maximum CO mixing ratio and the seasonal date at which that maximum occurs have a clear dependence on latitude. Outside of the polar regions, the annual maximum CO mixing ratio is greater and occurs earlier in the season the further south one goes. At 30°S latitude the annual maximum CO mixing ratio occurs at $L_s = 155°$, while at the equator the maximum is at $L_s = 180°$ and at 30°N it is at about $L_s = 215°$. Although the annual peak has lower amplitude at northern latitudes, it appears to more spread out in time covering a longer interval of seasonal dates. The overall seasonal dependence roughly follows the inverse of the annual cycle of surface pressure (or CO_2 abundance) as would be expected for a constant abundance (not mixing ratio) of CO, although there are differences. Comparing the two panels in Fig. 4 (the Viking 1 lander was at 22.5°N latitude), the annual peak mixing ratio of observed CO occur later than the annual minimum in surface pressure, and the observed CO mixing ratio does not have the pronounced minimum just before $L_s = 270°$ that would be expected given the annual maximum in surface pressure at that season. These differences are caused by the rate of latitudinal transport of CO, which is discussed further in Section 5.6.

4.2. Spatial variation of retrieved carbon monoxide

The maps in Fig. 5 show the spatial variation of CO volume mixing ratio at eight different seasonal dates throughout the Martian year. Some spatial smoothing has been performed to better show spatial patterns. The smoothing is performed by taking a box 45° in longitude by 15° in latitude centered on each retrieval. The
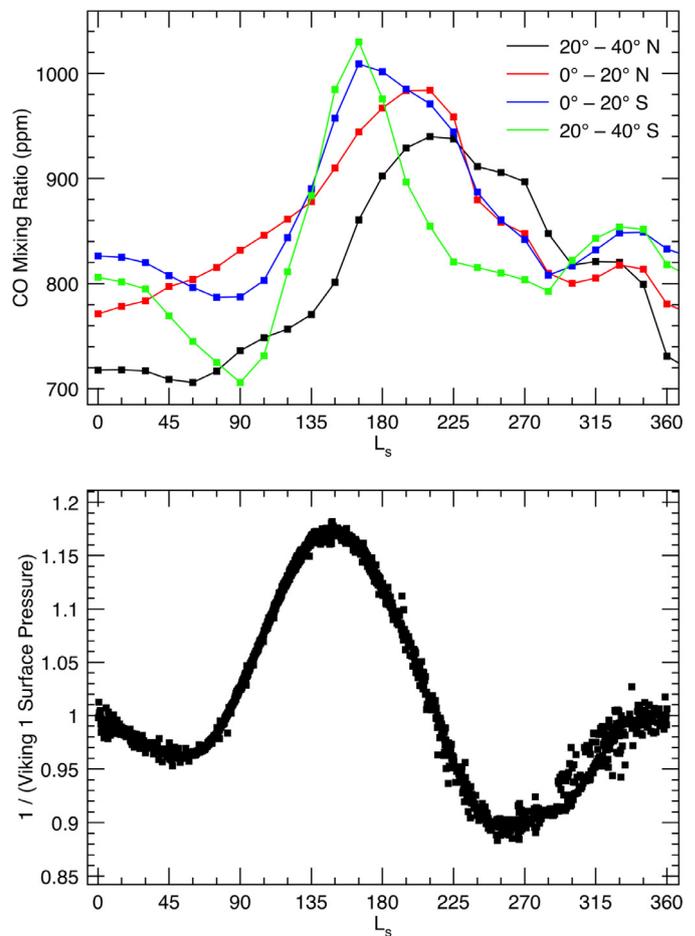
Fig. 4. (top) The retrieved CO mixing ratio from CRISM spectra as a function of season for four latitude bands. (bottom) Inverse of surface pressure measured by Viking Lander 1 (Tillman et al., 1993) scaled to unity at $L_s = 0°$.

highest 30% and lowest 30% of all points in the box are discarded, and the smoothed value is given as the average of the median 40% of the points in the averaging box.

Compared against the maps presented in Smith et al. (2009) that had the same spatial smoothing, the current improved retrieval shows noticeably less spatial variation in CO mixing ratio, especially as a function of longitude, which is a result of the improvements in the current retrieval algorithm. The overall lack of correlation of CO mixing ratio with topography in these maps supports our initial assumption that CO is well mixed with the background CO_2 gas. Still, there are systematic trends that are apparent in the maps. Most apparent are the strong latitudinal gradients in the summer hemisphere with the asymmetry noted earlier (stronger depletion in the southern summer polar region, but greater latitude extent of depletion at northern summer high latitudes).

In the summer hemispheres where there is CO depletion, there appears to be little longitudinal variation at high southern latitudes, while northern summer shows greater longitude variations with greater CO mixing ratio in the Utopia Planitia region than in Acidalia. In the winter hemispheres, the retrievals show generally greater CO mixing ratio in regions with low-lying topography. This is most apparent in Hellas basin during $L_s = 45°$–135°, but also shows up in the north as relative CO maxima around longitudes 30°, 165°, and 270°W in the season around $L_s = 270°$.

At lower latitudes the retrievals show more longitudinal variation overall in the season between $L_s = 135°$ and 225° when CO mixing ratio reaches its annual maximum and relatively little
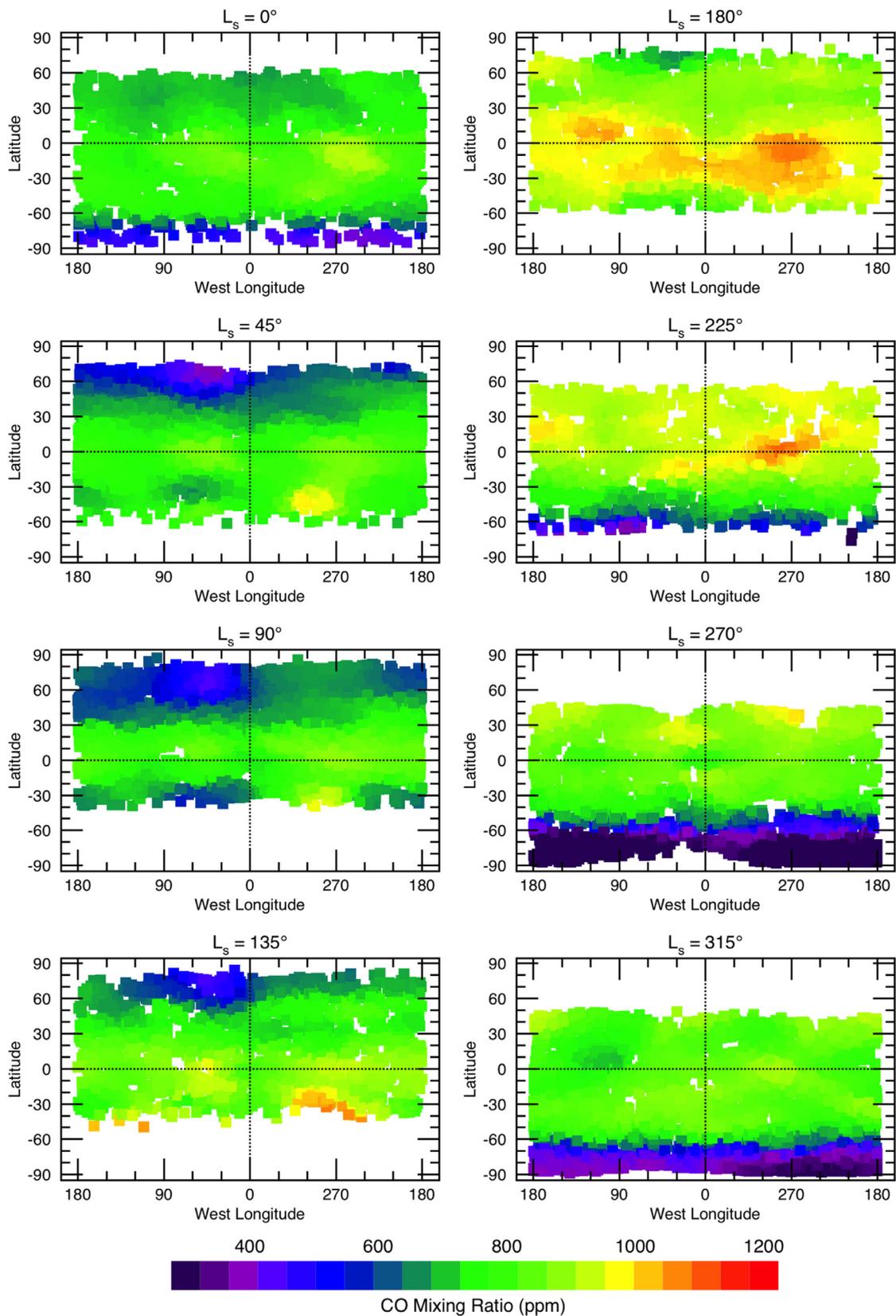
Fig. 5. Maps of CO mixing ratio retrieved from CRISM spectra for eight different seasons.
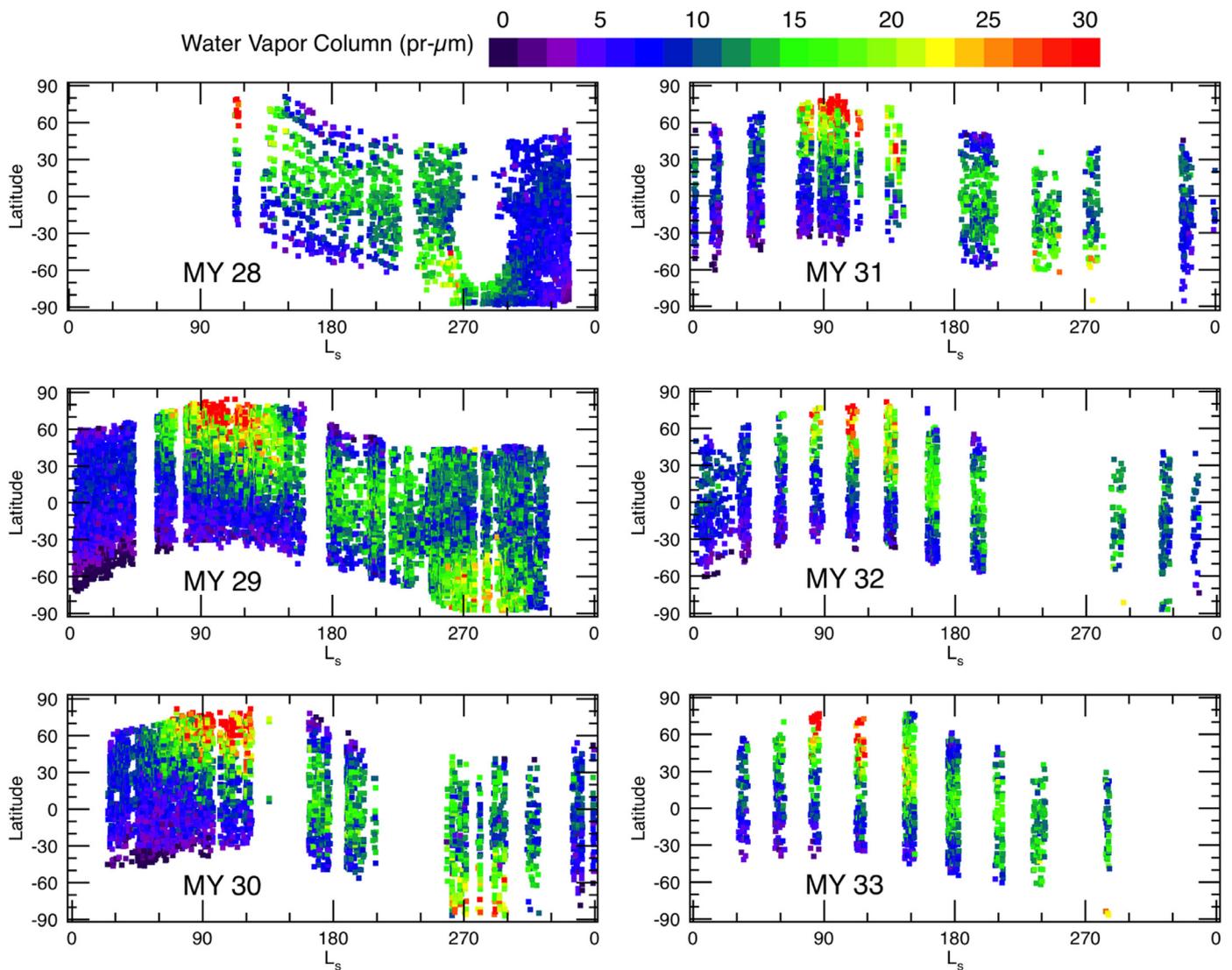
Fig. 6. The water vapor column abundance retrieved from CRISM spectra as a function of season, latitude, and Mars Year.

longitudinal variation in the season around $L_s = 0°$. In general, the region north of Hellas and the Margaritifer Terra region just east of the Valles Marineris tend to have higher CO mixing ratio than other low-latitude regions.

4.3. Interannual variation in water vapor

Fig. 6 shows the retrieved column abundance of water vapor as a function of season and latitude during the six Mars Years with CRISM observations. The familiar seasonal pattern observed previously by many instruments is apparent (e.g., Jakosky and Farmer, 1982; Smith, 2002, 2004; Smith et al., 2009; Fedorova et al., 2010; Trokhimovskiy et al., 2015). A strong maximum in water vapor abundance is observed at high latitudes during northern hemisphere summer with peak column abundance of about 50 precipitable-microns (pr-µm), which is somewhat less than the maximum values retrieved from TES and SPICAM spectra (Smith 2002, 2004; Trokhimovskiy et al., 2015). Water vapor abundance at high northerly latitudes rapidly decreases after $L_s = 120°$ with a corresponding increase at low northern latitudes reaching near 15 pr-µm. The southern hemisphere also shows a summertime maximum of water vapor at high latitudes, although it is notably weaker than in the north with maximum values reaching about 25 pr-µm. High-southern latitude water vapor abundance rapidly

decreases after $L_s = 300°$ and the entire southern hemisphere is relatively dry (less than about 5 pr–µm) after $L_s = 0°$.

The long record of CRISM observations enables the interannual variation of water vapor to be examined with a self-consistent set of retrievals. Despite the intermittent coverage over the most recent Mars Years because of limited use of the cryo-cooler, the seasonal trends are still apparent and can be compared. For the most part, the annual cycle is generally consistent from one Mars Year to the next.

Fig. 7 shows a direct comparison of the seasonal variation of water vapor between different Mars Years for three different latitude bands. The most significant exception is the apparent lack of water vapor during and in the immediate aftermath of the global-scale dust storm during MY 28. Retrieved water vapor abundance abruptly drops at the onset of the dust storm at MY 28, $L_s = 275°$ and remains low compared to other years until after MY 29, $L_s = 0°$. The decrease in the retrieved abundance of water vapor appears to be real since it lasts much longer than the elevated dust opacity from the global storm. This effect of the global dust storm on water vapor abundance was previously noted by Smith et al. (2009) and has been confirmed using SPICAM observations by Trokhimovskiy et al. (2015).

In both the northern and southern hemispheres, the increase of water vapor abundance at high latitudes during summer to its
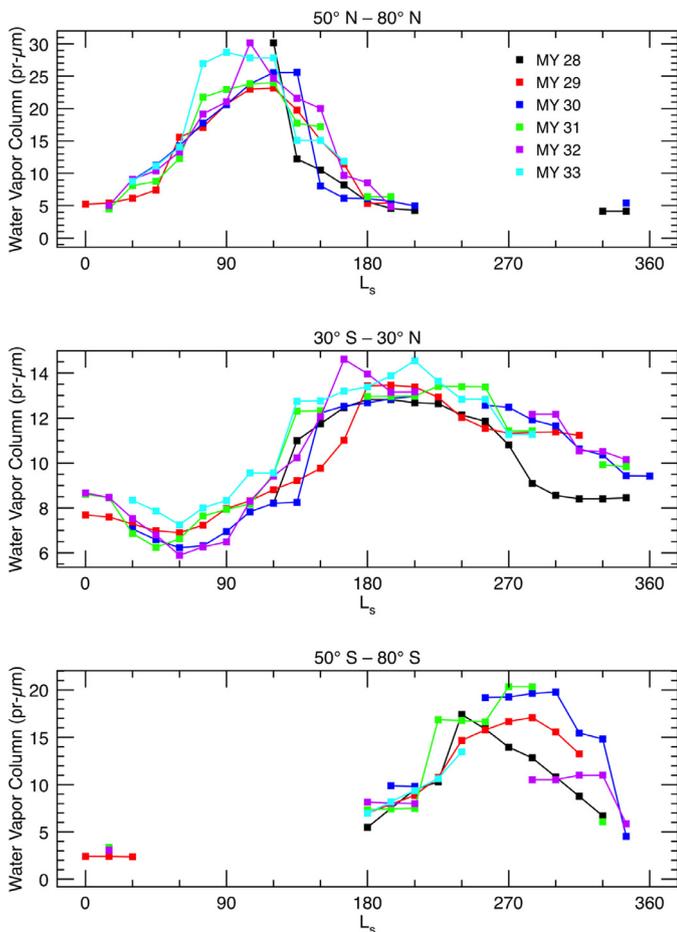
Fig. 7. The seasonal variation of retrieved water vapor in three different latitude bands for each Mars Year observed by CRISM.

annual maximum values is more consistent between different Mars Years than the decrease after the maximum is reached near summer solstice. The interannual variation appears to largely depend on the exact timing of when the summertime maximum is reached and when the water vapor abundance begins to decrease again.

It is interesting that the CRISM retrievals do not show the increased water vapor during MY 29, $L_s = 150°$–$160°$ at low latitudes reported by Trokhimovskiy et al. (2015) using SPICAM observations. This supports their interpretation that the high water vapor abundances from SPICAM are an observational artifact caused by preferential sampling of longitudes with systematically higher water vapor abundance. The CRISM retrievals also do not show any evidence of the 15% increase in water vapor at polar latitudes from MY 29 onward seen in SPICAM retrievals by Trokhimovskiy et al. (2015).

5. Comparison with GCM modeling results

5.1. GCM model description

The retrievals of CO and water vapor column abundance from CRISM described above are compared against simulations using the GEM-Mars General Circulation Model (Daerden et al., 2015; Neary and Daerden, 2017). The model is operated on a grid with a horizontal resolution of $4° \times 4°$ and with 103 vertical levels reaching from the surface to ~150 km. The model solves the primitive equations of atmospheric dynamics and calculates atmospheric heating and cooling rates by solar and IR radiation through atmospheric CO_2 and from dust and ice aerosols. The dynamical core, as well as

the entire modeling environment, was developed by the weather forecast department of Environment Canada and the model is fully parallelized. The geophysical boundary conditions are taken from observations. Physical parameterizations in the model include an interactive CO_2 condensation/surface pressure cycle, a thermal soil model including subsurface ice, interactive dust lifting schemes for saltation and dust devils, turbulent transport in the atmospheric surface layer and convective transport inside the planetary boundary layer (PBL), a low level blocking scheme, gravity wave drag, molecular diffusion, and atmospheric chemistry. Evaluation of the simulation of the dust cycle and the global circulation were first provided by Daerden et al. (2015) and Viscardy et al. (2016). Neary and Daerden (2017) provide a detailed model description and evaluation of the dynamical and chemical simulations.

5.2. Simulation of CO

Carbon monoxide (CO) is one of the chemical tracers in the model that is transported and that interacts with the other tracers through atmospheric chemistry. For this simulation, the chemical change is not applied to CO_2, CO, and O_2, and so CO is considered as a passive tracer. This was done to avoid small trends in the atmospheric CO content in multiannual simulations caused by the CO_2 stability problem (the recycling of CO and O_2 back into CO_2), which is not the focus of the present study. Given the relatively long chemical lifetime of CO of ~6 years (Krasnopolsky, 2007), this is a reasonable assumption on the scale of a few Mars years on which these simulations were performed.

CO was initialized to a uniform volume mixing ratio (vmr) of 800 ppm and transported through advection, vertical mixing, and molecular diffusion (see Neary and Daerden, 2017). When CO_2 condenses, the vmr of the non-condensable gases including CO are modified using a simple parameterization. This parameterization was updated from the version described in Neary and Daerden (2017) as explained below in Section 5.5.

Several approaches have been used in the past for modeling the polar enhancement of argon and the hemispheric transport of non-condensing species (Nelli et al., 2007; Forget et al., 2008; Lian et al., 2012; Sprague et al., 2012), but the present study is the first that directly compares model simulations to new spatially resolved retrievals of CO.

5.3. Simulation of the water cycle

The water cycle is simulated by GEM-Mars with reasonable agreement to observations and other models by applying a simple cloud treatment (Neary and Daerden, 2017). Water condenses into water ice if the partial pressure drops below the saturation pressure. Water ice is stored in a tracer that contains the vmr of the particles in the ice phase and is subject to advection and vertical mixing. For calculations regarding sedimentation and the radiative effect of water ice clouds, an ice particle radius of 4 μm was assumed, except in the sedimentation calculations below 10 km where an ice particle radius of 8 μm was assumed in order to simulate the stronger downward flux of water ice in the lowest scale height, as was indicated in measurements by the LIDAR on the Phoenix lander (Whiteway et al., 2009) and related microphysical simulations (Daerden et al., 2010). A change from Neary and Daerden (2017) is the definition of the spatial extent of the permanent water ice cap. The cap is now defined to be present on the surface for latitudes north of 80°N if the TES albedo (averaged over the $4° \times 4°$ grid cells) is larger than 0.23, and for latitudes between 70° and 80°N, also for longitudes between 90°W and 90°E (going through longitude 180°) if the albedo is larger than 0.24. The resulting spatial extent for the permanent water ice cap is shown in Fig. 8. Over the permanent cap the thermal inertia is set to
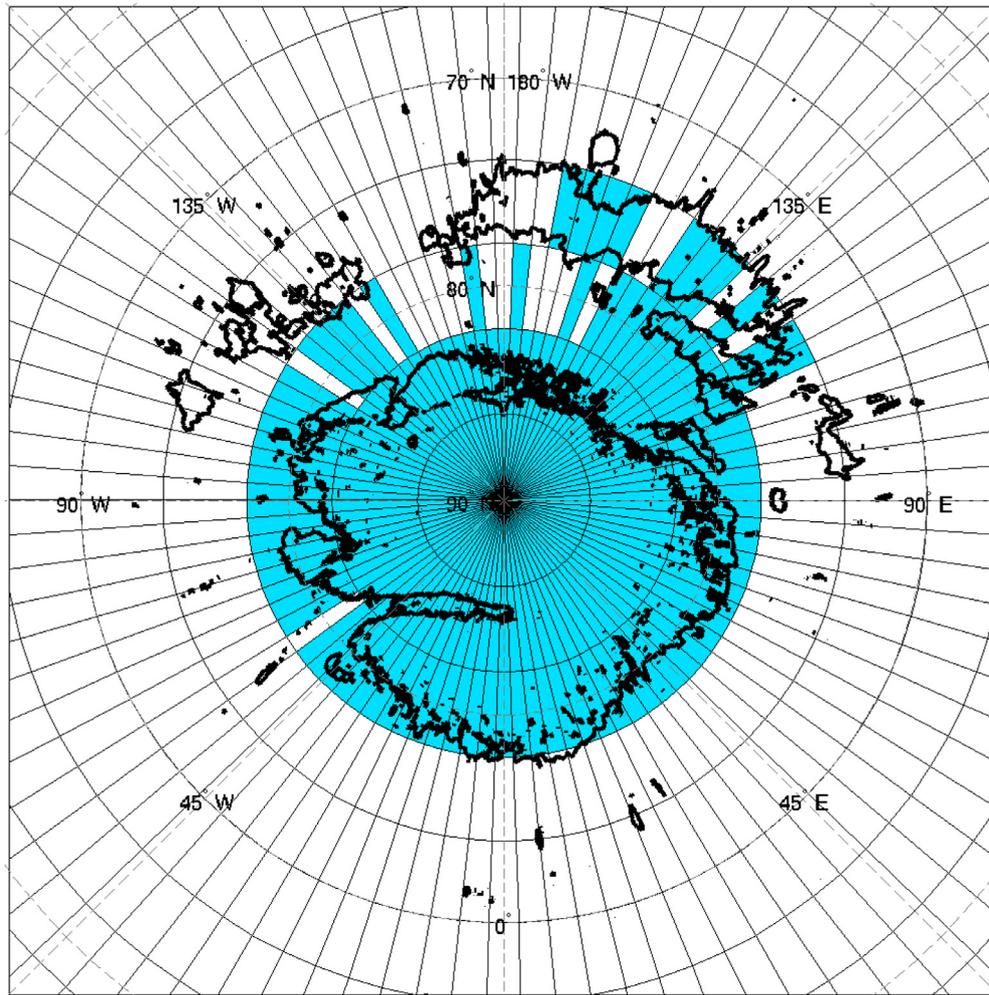
Fig. 8. Definition of the permanent water ice cap in the GEM-Mars model (blue) compared to TES albedo observations (black contours). (For interpretation of the references to color in this figure legend, the reader is referred to the web version of this article.)

$600\,J\,m^{-2}\,K^{-1}\,s^{-\frac{1}{2}}$. The albedo of surface water ice is set to 0.4. To avoid the formation of optically thick clouds over high northern latitudes during summer, which is a well-known problem in GCMs with radiative cloud feedbacks (e.g. Navarro et al., 2014), cloud formation is not allowed in the model for latitudes north of 70°N if the cloud optical depth falls below 0.2. This ad hoc solution leads to an improved simulation of cloud optical thickness in the model.

5.4. CO_2 surface exchange and the pressure cycle

In the GEM-Mars model, the local surface pressure change upon CO_2 condensation and sublimation is calculated from the temperature and pressure fields in the model following a similar parameterization as in Forget et al. (1998), with CO_2 ice precipitating to the surface within one model timestep (1/48th of a Mars solar day or sol). The calculation of the mass of condensing or sublimating CO_2 ice is based on the dynamical state and is not interactive with the chemical tracer for CO_2. The resulting surface pressure changes are returned to the dynamical core in which they are treated as a normal weather phenomenon (pressure drop or increase). The spread of the surface pressure changes over the planet occurs quite quickly in the model, on the scale of just a few hours or days. This approach is validated by the fact that the maximum in CO_2 surface ice mass as observed by the Gamma Ray Spectrometer (GRS) on Mars Odyssey (Kelly et al., 2006) lies within only a few degrees of L_s of the minimum in surface pressure as

observed by the Viking Landers (e.g., Haberle et al., 2008). This means that the atmospheric response to the polar CO_2 exchange is rapid both in reality and in the model. In GEM-Mars, the CO_2 surface ice mass variations are similar to those observed by GRS (Neary and Daerden, 2017) and to those simulated by other models (e.g., Haberle et al., 2008), and surface pressure variations are similar to measurements by surface landers (Neary and Daerden, 2017). A comparison of surface pressure as simulated in GEM-Mars to values retrieved from CRISM observations from orbit is presented in Fig. 9. For every time step and for every latitude where the solar zenith angle is less than 80°, the model fields are averaged over the longitudes that cover 2:00–4:00 PM local time (the time window during which the CRISM observations are taken), and the resulting averages are then binned over 20° latitude and 5° L_s. The individual CRISM retrievals are accumulated over all Mars Years, and then averaged over the same latitude and L_s bins. The overall agreement is good, although in a few regions the modeled surface pressure tends to be lower than in the CRISM retrievals. This could be due to the coarse model resolution. At all latitudes, the timing of the minimum and maximum pressure corresponds well.

5.5. Parameterization of non-condensable species

As explained above, the CO_2 ice/surface pressure cycle is currently calculated from the dynamical fields without modifying the tracers for atmospheric composition in the model. The total
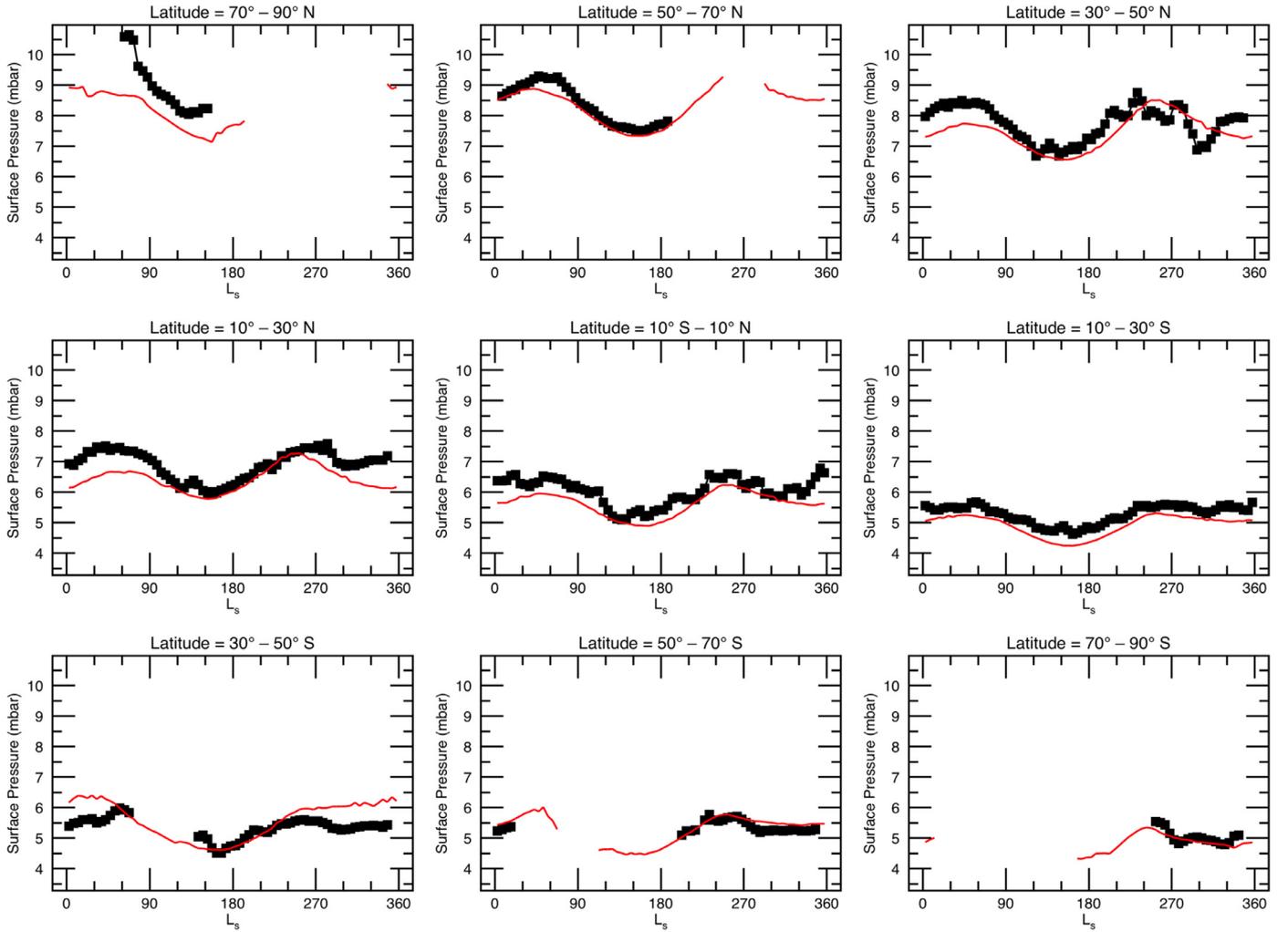
Fig. 9. Comparison of GEM-Mars model simulation of surface pressure (red line) with CRISM retrievals (black points). The model output is averaged over the local times observed by CRISM (2:00–4:00 PM). (For interpretation of the references to color in this figure legend, the reader is referred to the web version of this article.)

atmospheric mass then follows a seasonal trend, correlated with the surface pressure and anti-correlated with the CO_2 ice mass on the surface. The sum of total air mass and CO_2 ice mass is constant and equal to $\sim 2.9 \times 10^{16}$ kg, similar to values reported in Kelly et al. (2006), Guo et al. (2009), and Lian et al. (2012). In order to introduce spatial changes in air composition in relation to the CO_2 surface exchange, the following parameterization was developed. Wherever CO_2 is condensing, the vmr of CO_2 is updated at the vertical levels where ice is formed as $x'_{CO_2} = x_{CO_2} \times (1 - \alpha_c \times \frac{\Delta n_{d,ice}}{n_{d,air}})$ where $\Delta n_{d,\,ice}$ is the number density of CO_2 gas that condenses into ice in the grid cell, and $n_{d,\,air}$ is the number density of air in the grid cell. The parameter α_c is a proportionality factor for the condensation process. The vmr of the other species is then updated such that all vmrs sum up to unity, i.e. $x'_i = x_i \times \frac{1-x'_{CO_2}}{\sum_{i \neq CO_2} x_i}$. Wherever CO_2 ice is sublimating at the surface, the vmr of CO_2 is updated at all vertical levels as follows: $x'_{CO_2} = x_{CO_2} \times (1 - \alpha_s \times \frac{\Delta C_{ice}}{C_{air}})$. The amount ΔC_{ice} is the change in total column density of CO_2 ice particles (negative if ice sublimates). The factor $\frac{\Delta C_{ice}}{C_{air}}$ is identical to $\frac{\Delta p_s}{p_s}$, with p_s the surface pressure and Δp_s the change in surface pressure due to the sublimation of CO_2 ice. As before, α_s is a proportionality factor for the sublimation process. The vmr of the other species is updated as before to sum up to unity.

This simple approach causes seasonal variations in the total atmospheric content of the non-condensing species of $\sim 7\%$, which is much less than the enrichment factors seen in observations (Sprague et al., 2004, 2007, 2012). The proportionality factors α_c and α_s are chosen such that on an annual basis the atmospheric content of the species is conserved. Extensive tests led to the following optimal values: $\alpha_c = 0.025$, $\alpha_s = 0.030$. The fact that the two parameters do not have the same value is probably related to the differences in vertical distribution and the time scales of the processes of condensation and sublimation.

With this parameterization, strong spatial gradients comparable to observations are introduced in the model following local formation or sublimation of CO_2 ice. Enhancement factors for polar argon (Neary and Daerden, 2017) are similar to those reported in other models (Sprague et al., 2004, 2007, 2012; Lian et al., 2012). Below we will present and discuss the simulation of CO on the global scale and the comparison to the new dataset of CRISM retrievals described in Section 4.

5.6. Comparison of the observed and modeled CO seasonal cycle

The annual simulation of the CO column abundance relative to that of CO_2 for local times corresponding to the CRISM observations (averaged over 2:00–4:00 PM local time) is shown in Fig. 10. In the south polar region during local winter, roughly between
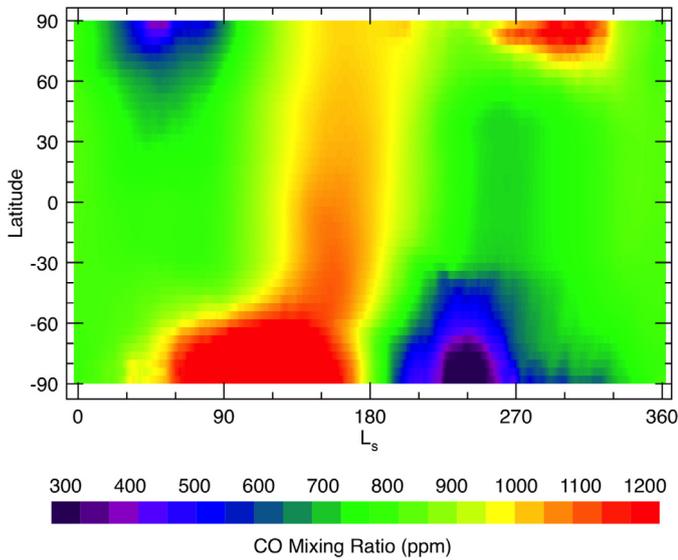
Fig. 10. GEM-Mars model simulation of CO mixing ratio averaged over the local times observed by CRISM (2:00–4:00 PM).

$L_s = 30°$ and $150°$, enrichment of CO occurs as CO_2 is increasingly condensed onto the surface. The enrichment increases with time, until the enriched air starts "leaking" from the south polar region, roughly between $L_s = 120°$ and $180°$. This leaking is related to the breaking of the polar vortex towards the end of the winter, and occurs primarily through the topographically low Hellas and Argyre basins. The enriched air is then transported quite quickly to lower latitudes and into the northern hemisphere. The pole-to-pole transport takes roughly $30°$ in L_s ($\sim$60 sols). In the north polar region, a similar enrichment occurs during local winter, although it is much less strong because of the smaller CO_2 ice mass that forms at the north pole. Leaking of the enriched air at the end of the winter followed by pole-to-pole transport is also very much reduced compared to the south.

At both poles the enrichment during local winter is followed by a depletion of CO during local summer, the effect again being much stronger in the south compared to the north. The explanation is again the larger CO_2 ice mass that is sublimating in the south compared to the north. In the south, the depletion is so strong that it propagates towards lower latitudes and into the northern hemisphere, to the edge of the northern seasonal cap.

For a detailed comparison of the model simulations to the CRISM retrievals, both datasets were averaged over 20° latitude and 5° L_s as before (Fig. 11). In almost all cases the model simulation falls within the one-sigma variability of the CRISM retrievals
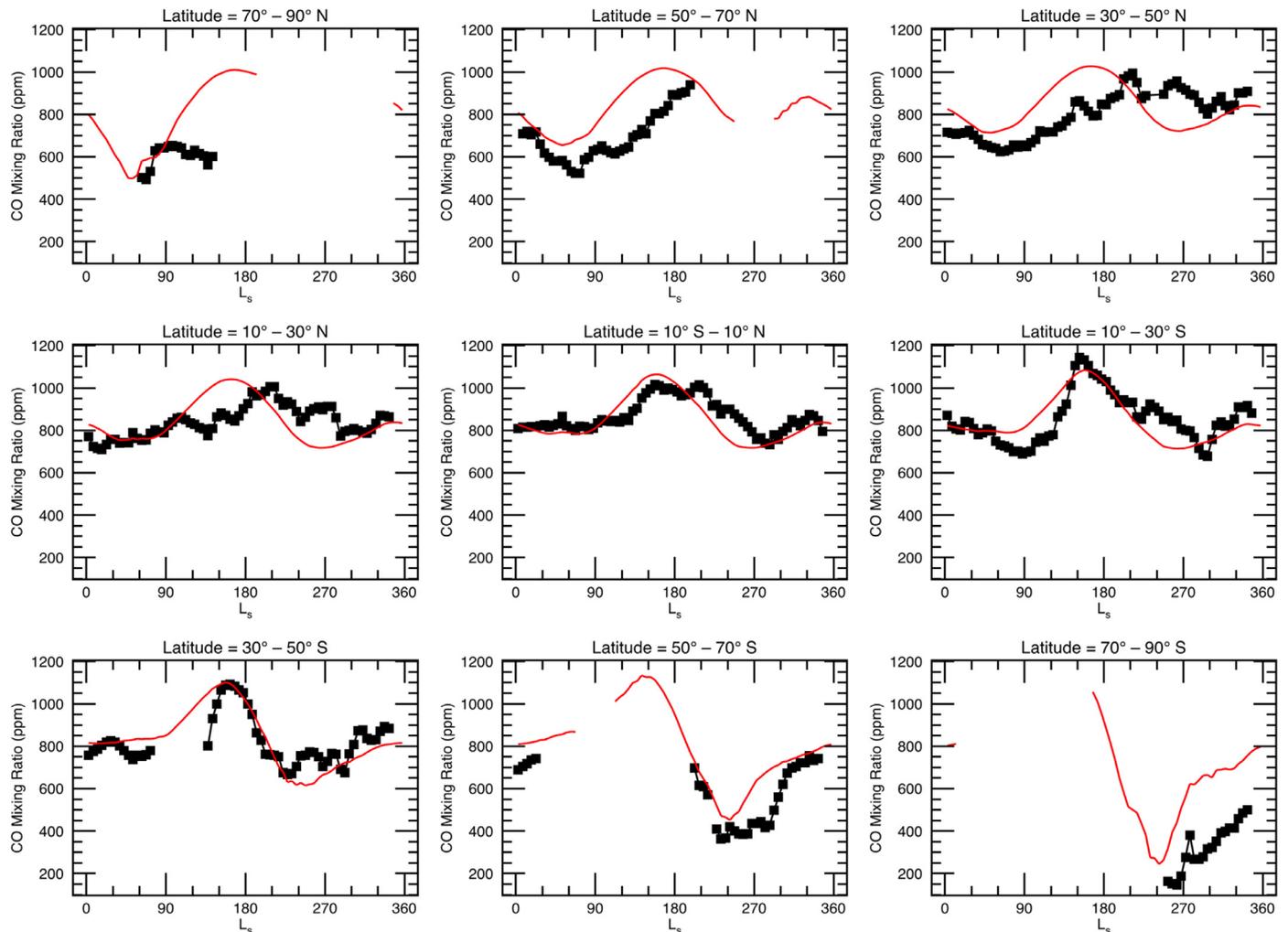
Fig. 11. Comparison of GEM-Mars model simulation of CO mixing ratio (red line) with CRISM retrievals (black points). The model output is averaged over the local times observed by CRISM (2:00–4:00 PM). The estimated uncertainty in the binned retrievals is 100 ppm. (For interpretation of the references to color in this figure legend, the reader is referred to the web version of this article.)
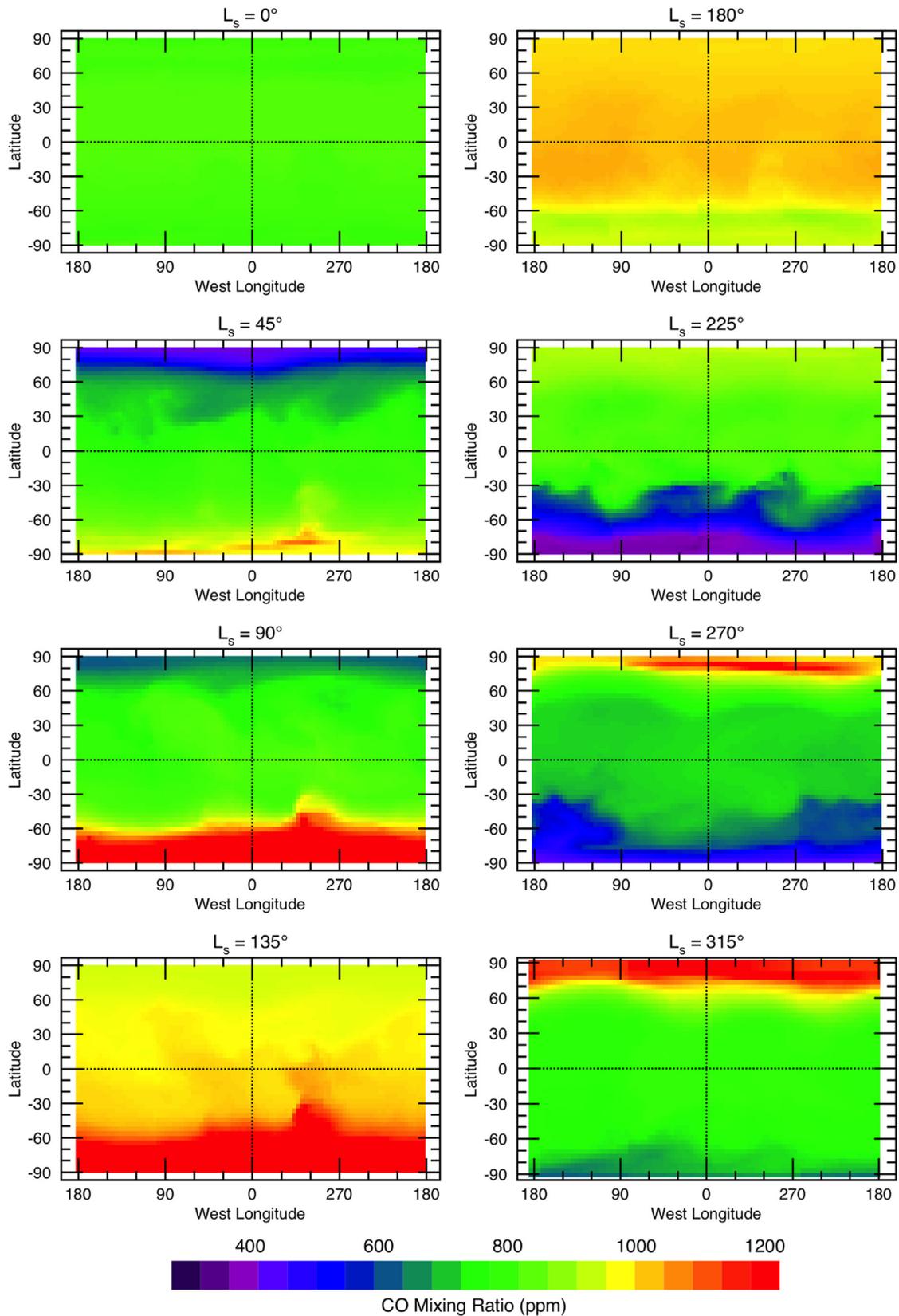
Fig. 12. Maps of CO mixing ratio simulated by the GEM-Mars model for eight different seasons.

when combining retrieval uncertainty and biases in spatial and seasonal sampling, but there are still some significant trends in the retrievals that the model does not reproduce. The main differences are:

- At polar latitudes at the end of the polar winter, the CO in the model builds up more rapidly than in the retrievals.
- In the southern hemisphere between 10° and 50° S latitude, a local minimum in the retrieved CO is seen around winter solstice ($L_s = 90°$) that is not present in the model simulation.
- From the equator to the north, there is an increasing time shift for the annual maximum CO value, with the model being at an earlier L_s than the retrievals. The time shift increases with latitude to as much as 60° of L_s at 50°–70°N. The retrievals show that a latitude gradient is present for a longer time than in the simulations. As the modeled and retrieved surface pressure follow each other closely, it appears that the rate at which enriched CO mixes from the southern hemisphere toward northern latitudes is much slower than the rate at which the change in surface pressure propagates to the north.

As a result, the CO vmr remains high in the CRISM retrievals during $L_s = 180°–270°$ at northern latitudes, while it drops in the model simulation due to the mixing of depleted air after sublimation of the southern seasonal cap. The model simulations of Lefèvre and Forget (2009) and Lian et al. (2012) are very similar to that of the GEM-Mars model, indicating that the biases reported here highlight a common shortcoming of GCMs.

In general, the GEM-Mars model results for CO vmr (Fig. 12) show somewhat less longitudinal variation than that seen in the CRISM retrievals (Fig. 5), although several key features are apparent. In particular, the model results show the same enhancement in CO mixing ratio in the winter hemisphere mid-latitude regions with low topography. As mentioned earlier, these regions (Hellas and Argyre during $L_s = 90°–135°$, and to a lesser extent the areas around longitudes 30°, 165°, and 270°W in the season after $L_s = 270°$) are where air enriched with CO leaks out of the polar regions as a result of the breaking of the polar vortex towards the end of the winter.

5.7. Comparison of the observed and modeled water cycle

The annual simulation of the vertical column of water vapor for local times corresponding to CRISM observations (averaged over 2:00–4:00 PM local time) is shown in Fig. 13. The main features of the water cycle are simulated in GEM-Mars with reasonable precision: the peak release of water vapor from the permanent cap during northern summer, the release from sublimation of surface ice at sub-polar latitudes during northern winter, the transport to lower latitudes, and the formation of a peak in the south at the end of local winter by sublimation of water that was condensed on the south polar seasonal cap.

For a more detailed comparison of the model simulations to the CRISM retrievals, all Mars Years from both datasets were again averaged over 20° latitude and 5° L_s (Fig. 14). For the first half of the year ($L_s = 0°–180°$) the model simulation falls within the one-sigma variability of the CRISM retrievals, except at northern mid-to-high latitudes around $L_s = 90°$. This is likely related to an underestimation of the sub-polar surface water ice deposits in the current version of GEM-Mars.

It is also worth noting that the polar properties in GEM-Mars (thermal inertia and surface water ice albedo) were set to reproduce the peak water column at the pole as retrieved by CRISM, which is lower than the peak values retrieved using TES spectra (Smith, 2004). Reducing the water ice albedo in the model from 0.40 to 0.38 would lead to a polar water release that matches
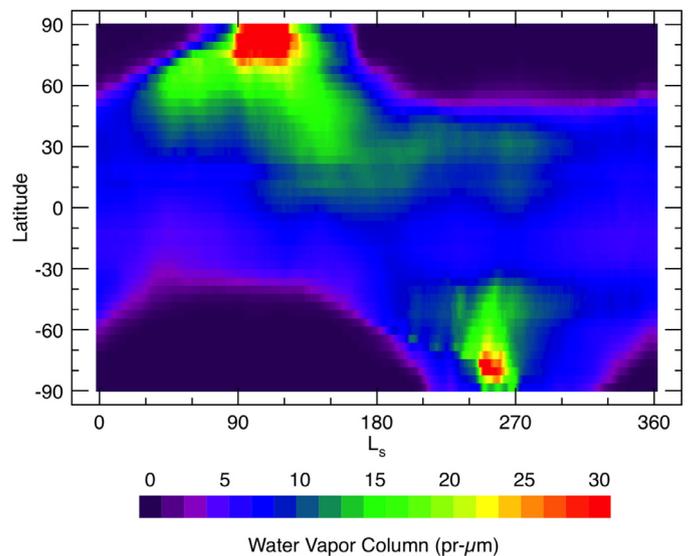
Fig. 13. GEM-Mars model simulation of water vapor column abundance averaged over the local times observed by CRISM (2:00–4:00 PM).

the TES retrievals, and would also improve the biases between the model and CRISM retrievals at 30°–70°N.

In the second half of the year ($L_s = 180°–360°$) the differences between the model results and CRISM retrievals are larger than they are in the first half of the year. Specifically, for latitudes between 30°S and 50°N the GEM-Mars water column is 15–40% lower than the CRISM retrievals. This may be explained by either an excessive formation of ice in the model or by the north to south transport of water in the model being too fast. Comparisons with TES retrievals of ice optical depth and surface temperature indicate that the model does not simulate excessive ice clouds or surface water ice in this season (not shown) so the bias seems to be transport-related.

At south polar latitudes, the modeled peak of water vapor after the sublimation of the seasonal cap is high and short compared to CRISM retrievals. This is in part related to an imperfect implementation of the south polar permanent CO_2 cap as a result of the spatial resolution of the model. It is hard to simulate the long yet weak tail of CO_2 ice mass on the surface as observed by GRS between $L_s = 250°$ and 280°, where the Ames model also experienced problems (Haberle et al., 2008). The difference in duration of the water peak is likely related to the problem in CO seen in the same region and time of year. This may indicate that mixing in the model at these latitudes is too strong, explaining why in the CRISM retrievals the released water vapor remains confined to high latitudes much longer than in the model simulation.

6. Summary

The continued successful operation of the Mars Reconnaissance Orbiter and the CRISM instrument have extended the existing interannual record of water vapor retrievals and enabled a detailed global description of the seasonal and spatial distribution of CO in the Mars atmosphere. Comparison of the CRISM retrieval results with the output from the GEM-Mars GCM provides insight into the underlying physical processes and identifies areas where the model and the retrieval algorithms could be improved.

The CRISM retrievals of water vapor reveal only modest interannual variations. The most significant of those is the apparent lack of water vapor during and in the immediate aftermath of the global scale dust storm during MY 28, which has also been noted in previous studies (Smith et al., 2009; Trokhimovskiy et al., 2015).
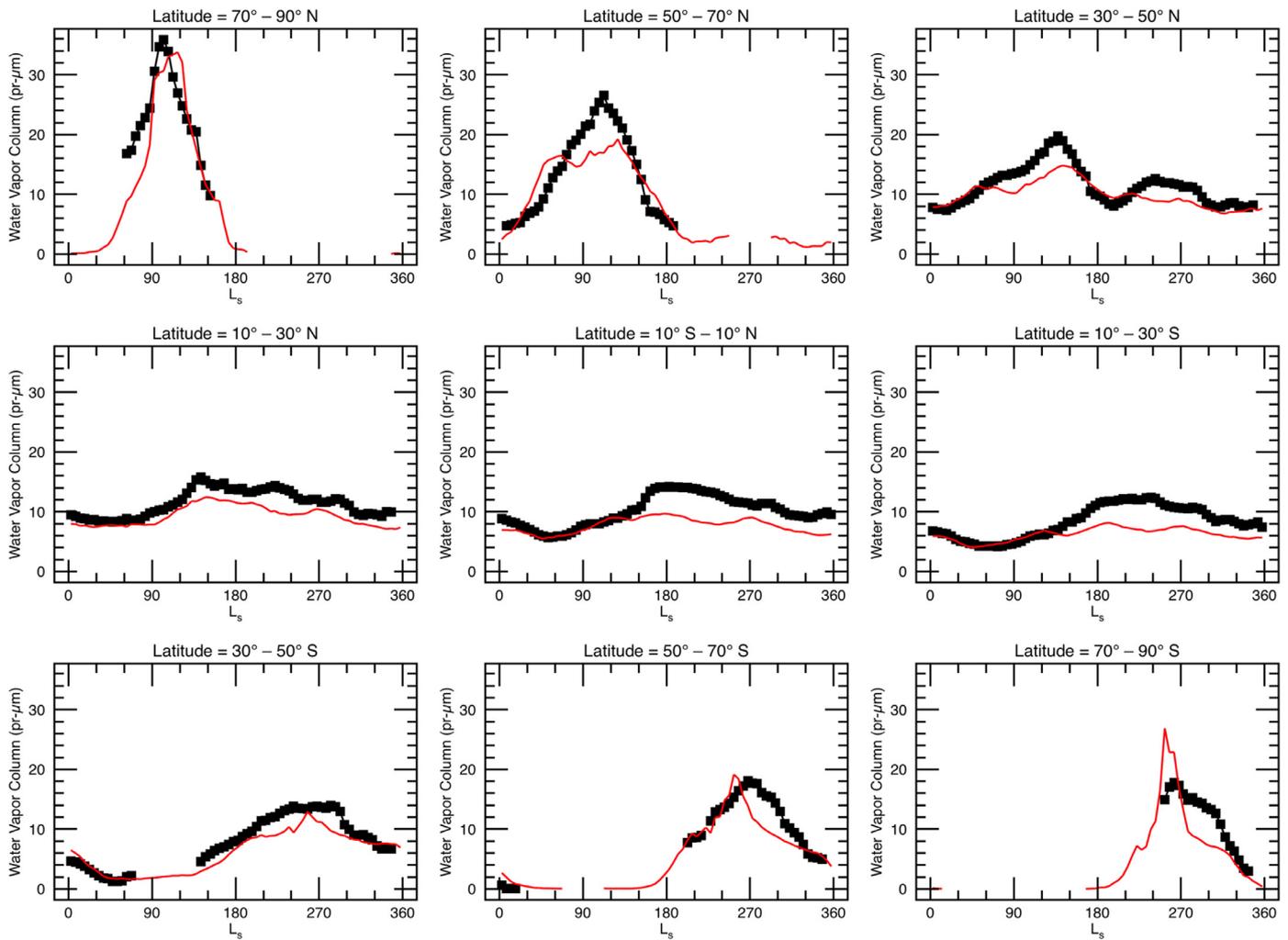
Fig. 14. Comparison of GEM-Mars model simulation of water vapor column abundance (red line) with CRISM retrievals (black points). The model output is averaged over the local times observed by CRISM (2:00–4:00 PM). The estimated uncertainty in the binned retrievals is 2 pr-μm. (For interpretation of the references to color in this figure legend, the reader is referred to the web version of this article.)

The CRISM retrievals also indicate some variation from one Mars Year to the next in the timing of the summertime high-latitude maximum in water vapor abundance in each hemisphere and its subsequent decrease.

The CRISM retrievals of carbon monoxide reveal the globally averaged mixing ratio to be near 800 ppm, but with strong seasonal and spatial variations, especially at high latitudes. At low latitudes, the carbon monoxide mixing ratio varies in response to the mean seasonal cycle of surface pressure and shows little variation with topography. At high latitudes, carbon monoxide is depleted in the summer hemisphere by a factor of two or more, while in the winter hemisphere there is relatively higher mixing ratio in regions with low-lying topography.

Comparison of the CRISM retrievals with the results of the GEM-Mars general circulation model shows good overall agreement. In particular, the seasonal and spatial variation of CO retrieved from CRISM generally follows the modeled variations for a non-condensable gas from GEM-Mars. The model results explain the observed leaking of enriched air into regions of low topography as the result of breaking of the polar vortex toward the end of winter. The observation that the seasonal variation of CO is much greater in the south polar region than in the north is shown by the model to be directly related to the much larger mass of CO_2

ice in the southern cap. Differences between the CRISM retrievals and the model results indicate that the observed rate of CO mixing is slower than in GEM-Mars and other models (Lefèvre and Forget 2009; Lian et al., 2012).

Continued observations by CRISM will further extend the existing multi-year record of water vapor and carbon monoxide retrievals and will provide a valuable link to upcoming observations by the Trace Gas Orbiter (e.g., Korablev et al., 2014; Vandaele et al., 2015).

Acknowledgments

References

Berk, A., Bernstein, L.S., Anderson, G.P., et al., 1998. MODTRAN cloud and multiple scattering upgrades with application to AVIRIS. Remote Sens. Environ. 65, 367–375.

Billebaud, F., Brillet, J., Lellouch, E., et al., 2009. Observations of CO in the atmosphere of Mars with PFS onboard Mars Express. Planet. Space Sci. 57, 1446–1457.

Brown, L.R., Humphrey, C.M., Gamache, R.R., 2007. CO_2-broadened water in the pure rotation and n2 fundamental regions. J. Mol. Spectrosc. 246, 1–21.

Clancy, R.T., Muhlman, D.O., Berge, G.L., 1990. Global changes in the 0–70 km thermal structure of the Mars atmosphere derived from 1975 to 1989 microwave CO spectra. J. Geophys. Res. 95, 14543–14554.

Clancy, R.T., Wolff, M.J., Christensen, P.R., 2003. Mars aerosol studies with the MGS-TES emission phase function observations: optical depths, particle sizes, and ice cloud types versus latitude and solar longitude. J. Geophys. Res. 108 (E9), 5098. doi:10.1029/2003JE002058.

Cull, S., Arvidson, R.E., Mellon, M., et al., 2010. Seasonal H_2O and CO_2 ice cycles at the Mars Phoenix landing site: 1. Prelanding CRISM and HiRISE observations. J. Geophys. Res. 115, E00D16. doi:10.1029/2009JE003340.

Daerden, F., Whiteway, J.A., Davy, R., et al., 2010. Simulating observed boundary layer clouds on Mars. Geophys. Res. Lett. 37, L04203. doi:10.1029/2009GL041523.

Daerden, F., Whiteway, J.A., Neary, L., et al., 2015. A solar escalator on Mars: self-lifting of dust layers by radiative heating. Geophys. Res. Lett. 42, 73197326. doi:10.1002/2015GL064892.

Encrenaz, T., Fouchet, T., Melchiorri, R., et al., 2006. Seasonal variations of the Martian CO over Hellas as observed by OMEGA/Mars Express. Astron. Astrophys. 459, 265–270.

Fedorova, A.A., Korablev, O.I., Bertaux, J.L., et al., 2006. Mars water vapor abundance from SPICAM IR spectrometer: seasonal and geographic distributions. J. Geophys. Res. 111, E09S08. doi:10.1029/2006JE002695.

Fedorova, A.A., Trokhimovskiy, A.Y., Korablev, O., Montmessin, F., 2010. Viking observation of water vapor on Mars: revision from up-to-date spectroscopy and atmospheric models. Icarus 208, 156–164.

Forget, F., Hourdin, F., Talagrand, O., 1998. CO_2 snowfall on Mars: simulation with a general circulation model. Icarus 131, 302–316.

Forget, F., Millour, E., Montabone, L., Lefevre, F., 2008. Non condensable gas enrichment and depletion in the Martian polar regions. Paper presented at Third International Workshop on the Mars Atmosphere: Modeling and Observations, Lunar and Planet. Inst. Williamsburg, VA, 10–13.

Fouchet, T., et al., 2007. Martian water vapor: Mars Express PFS/LW observations. Icarus 190, 32–49.

Gamache, R.R., Neshyba, S.P., Plateaux, J.J., et al., 1995. CO_2-broadening of water vapor lines. J. Mol. Spectrosc. 170, 131–151.

Goody, R.M., Yung, Y.L., 1989. Atmospheric Radiation: Theoretical Basis. Oxford University Press, New York.

Guo, X., Lawson, W.G., Richardson, M.I., Toigo, A., 2009. Fitting the Viking lander surface pressure cycle with a Mars General Circulation Model. J. Geophys. Res. 114, E07006. doi:10.1029/2008JE003302.

Haberle, R.M., Forget, F., Colaprete, A., et al., 2008. The effect of ground ice on the Martian seasonal CO_2 cycle. Planet. Space Sci. 56, 251–255. doi:10.1016/j.pss.2007.08.006.

Jakosky, B.M., Farmer, C.B., 1982. The seasonal and global behavior of water vapor in the Mars atmosphere: complete global results of the Viking atmospheric water detector experiment. J. Geophys. Res. 87, 2999–3019.

Kelly, N.J., Boynton, W.V., Kerry, K., et al., 2006. Seasonal polar carbon dioxide frost on Mars: CO_2 mass and columnar thickness distribution. J. Geophys. Res. 111, E03S07. doi:10.1029/2006JE002678.

Korablev, O., Trokhimovsky, A., Grigoriev, A.V., et al., 2014. Three infrared spectrometers, an atmospheric chemistry suite for the ExoMars 2016 trace gas orbiter. J. Appl. Remote Sens. doi:10.1117/1.JRS.8.084983.

Krasnopolsky, V.A., 2003. Spectroscopic mapping of Mars CO mixing ratio: detection of north-south asymmetry. J. Geophys. Res. 108, 5010. doi:10.1029/2002JE001926.

Krasnopolsky, V.A., 2007. Long-term spectroscopic observations of Mars using IRTF/CSHELL: mapping of O_2 dayglow, CO, and search for CH4. Icarus 190, 93–102.

Lacis, A.A., Oinas, V., 1991. A description of the correlated-k distribution method for modeling nongray gaseous absorption, thermal emission, and multiple scattering in vertically inhomogeneous atmospheres. J. Geophys. Res. 96, 9027–9063.

Lefèvre, F., Forget, F., 2009. Observed variations of methane on Mars unexplained by known atmospheric chemistry and physics. Nature 460, 720–723. doi:10.1038/nature08228.

Lellouch, E., Paubert, G., Encrenaz, T., 1991. Mapping of CO millimeter-wave lines in Mars atmosphere: the spatial distribution of carbon monoxide on Mars. Planet. Space Sci. 39, 219–224.

Lian, Y., Richardson, M.I., Newman, C.E., et al., 2012. The Ashima/MIT Mars GCM and argon in the martian atmosphere. Icarus 218, 1043–1070. doi:10.1016/j.icarus.2012.02.012.

Mahaffy, P.R., Webster, C.R., Atreya, S.K., et al., 2013. Abundance and isotopic composition of gases in the martian atmosphere from the Curiosity rover. Science 341, 263–266.

Maltagliati, L., Titov, D.V., Encrenaz, T., et al., 2008. Observations of atmospheric water vapor above the Tharsis volcanoes on Mars with the OMEGA/MEX imaging spectrometer. Icarus 194, 53–64.

Maltagliati, L., Titov, D.V., Encrenaz, T., et al., 2011. Annual survey of water vapor behavior from the OMEGA mapping spectrometer onboard Mars Express. Icarus 213, 480–495.

Melchiorri, R., et al., 2007. Water vapor mapping on Mars using OMEGA/Mars Express. Planet. Space Sci. 55, 333–342.

Murchie, S., et al., 2007. Compact Reconnaissance Imaging Spectrometer for Mars (CRISM) on Mars Reconnaissance Orbiter (MRO). J. Geophys. Res. 112, E05S03. doi:10.1029/2006JE002682.

Navarro, T., Madeleine, J.-B., Forget, F., et al., 2014. Global climate modeling of the Martian water cycle with improved microphysics and radiatively active water ice clouds. J. Geophys. Res. Planets 119, 1479–1495. doi:10.1002/2013JE004550.

Neary, L., Daerden, F., 2017. The GEM-Mars general circulation model for mars: description and evaluation. Icarus doi:10.1016/j.icarus.2017.09.028.

Nelli, S., Murphy, J.R., Sprague, A.L., et al., 2007. Dissecting the polar dichotomy of the noncondensable gas enhancement on Mars using the NASA Ames Mars general circulation model. J. Geophys. Res. 112, E08S91. doi:10.1029/2006JE002849.

Pelkey, S.M., et al., 2007. CRISM multispectral summary products: Para- meterizing mineral diversity on Mars from reflectance. J. Geophys. Res. 112, E08S14. doi:10.1029/2006JE002831.

Rothman, L.S., Gordon, I.E., Babikov, Y., et al., 2013. The HITRAN2012 molecular spectroscopic database. J. Quant. Spectr. Rad. Transf. 130, 4–50.

Smith, M.D., 2002. The annual cycle of water vapor on Mars as observed by the Thermal Emission Spectrometer. J. Geophys. Res. 107 (E11), 5115. doi:10.1029/2001JE001522.

Smith, M.D., 2004. Interannual variability in TES atmospheric observations of Mars during 1999–2003. Icarus 167, 148–165. http://dx.doi.org/10.1016/j.icarus.2003.09.010.

Smith, M.D., Wolff, M.J., Clancy, R.T., Murchie, S.L., 2009. Compact Reconnaissance Imaging Spectrometer observations of water vapor and carbon monoxide. J. Geophys. Res. 114, E00D03. doi:10.1029/2008JE003288.

Sung, K., Varanasi, P., 2005. CO_2-broadened half-widths and CO_2-induced line shifts of $^{12}C^{16}O$ relevant to the atmospheric spectra of Venus and Mars. J. Quant. Spectrosc. Radiat. Transf. 91, 319–332.

Sprague, A.L., Boynton, W.V., Kerry, K.E., et al., 2004. Mars' south polar Ar enhancement: a tracer for south polar seasonal meridional mixing. Science 306, 1364–1367.

Sprague, A.L., Boynton, W.V., Kerry, K.E., et al., 2007. Mars' atmospheric argon: tracer for understanding Martian atmospheric circulation and dynamics. J. Geophys. Res. 112, E03S02. doi:10.1029/2005JE002597.

Sprague, A.L., Boynton, W.V., Forget, F., et al., 2012. Interannual similarity and variation in seasonal circulation of Mars' atmospheric Ar as seen by the Gamma Ray Spectrometer on Mars Odyssey. J. Geophys. Res. 117, E04005. doi:10.1029/2011JE003873.

Thomas, G.E., Stamnes, K., 1999. Radiative Transfer in the Atmosphere and Ocean. Cambridge University Press, Cambridge.

Tillman, J.E., Johnson, N.C., Guttorp, P., Percival, D.B., 1993. The Martian annual atmospheric pressure cycle: years without great dust storms. J. Geophys. Res. 98 (E6), 10963–10971.

Trokhimovskiy, A., Fedorova, A., Korablev, O., et al., 2015. Mars' water vapor mapping by the SPICAM IR spectrometer: five martian years of observations. Icarus 251, 50–64.

Tschimmel, M., Ignatiev, N.I., Titov, D.V., et al., 2008. Investigation of water vapor on Mars with PFS/SW of Mars Express. Icarus 195, 557–575.

Vandaele, A.C., Neefs, E., Drummond, R., et al., 2015. Science objectives and performances of NOMAD, a spectrometer suite for the ExoMars TGO mission. Planet. Space Sci. 119, 233–249.

Varanasi, P., 1975. Measurement of line widths of CO of planetary interest at low temperatures. J. Quant. Spectrosc. Radiat. Transf. 15, 191–196.

Viscardy, S., Daerden, F., Neary, L., 2016. Formation of layers of methane in the atmosphere of Mars after surface release. Geophys. Res. Lett. 43 (5), 1868–1875. doi:10.1002/2015GL067443.

Whiteway, J.A., Komguem, L., Dickinson, C., et al., 2009. Mars water-ice clouds and precipitation. Science 325, 68–70. doi:10.1126/science.1172344.

Wolff, M.J., Clancy, R.T., 2003. Constraints on the size of martian aerosols from Thermal Emission Spectrometer observations. J. Geophys. Res. 108, 5097. http://dx.doi.org/10.1029/2003JE002057.

Wolff, M.J., et al., 2006. Constraints on dust aerosols from the Mars Exploration Rovers using MGS overflights and Mini-TES. J. Geophys. Res. 111, E12S17. http://dx.doi.org/10.1029/2006JE002786.

Wolff, M.J., et al., 2009. Wavelength dependence of dust aerosol single scattering albedo as observed by the Compact Reconnaissance Imaging Spectrometer. J. Geophys. Res. 114, E00D04. http://dx.doi.org/10.1029/2009JE00350.

Zurek, R.W., Smrekar, S.E., 2007. An overview of the Mars Reconnaissance Orbiter (MRO) science mission. J. Geophys. Res. 112, E05S01. doi:10.1029/2006JE002701.